Parallel Transmit and Receive Technology in High-Field Magnetic Resonance Neuroimaging

Andrew G. Webb,[1] Christopher M. Collins[2]

[1] C.J. Gorter Center for High Field MRI, Department of Radiology, Leiden University Medical Center, Leiden, The Netherlands

[2] Department of Radiology, The Pennsylvania State University College of Medicine, Hershey, PA

Received 30 September 2009; accepted 4 December 2009

ABSTRACT: The major radiofrequency engineering challenges of high-field MR neuroimaging are as follows: (1) to produce a strong, homogeneous transmit B_1 field, while remaining within regulatory guidelines for tissue power deposition and (2) to receive the signal with the maximum signal-to-noise and the greatest flexibility in terms of utilizing the benefits of parallel imaging. Borrowing from developments in electromagnetic hyperthermia, the first challenge has been met by the use of transmit arrays, in which the input power to each element of the array can be varied in terms of magnitude and phase. Optimization of these parameters, as well as the form of the applied RF pulse, leads to very homogeneous B_1 fields throughout the brain. The design of large receive arrays, using impedance-mismatched preamplifiers and geometrical overlap for interelement isolation, has resulted in significant sensitivity improvements as well as large acceleration factors in parallel imaging. Int J Imaging Syst Technol, 20, 2–13, 2010; Published online in Wiley InterScience (www.interscience.wiley.com). DOI 10.1002/ima.20219

Key words: high-field MRI; parallel array; receiver coils

I. CLINICAL POTENTIAL OF HIGH-FIELD MAGNETIC RESONANCE NEUROIMAGING

Magnetic resonance imaging (MRI) has a long and successful history in diagnosing and characterizing chronic neurodegenerative diseases such as Alzheimer's, Parkinson's, cerebral autosomal dominant arteriopathy with subcortical infarcts and leukoencephalopathy (CADASIL), multiple sclerosis (MS), and cerebral amyloid angiopathy (CAA). The advent of commercial high-field (7 T and above) MRI systems has already resulted in substantial information on such diseases, which was not accessible at lower fields. In addition to the general advantage of increased signal-to-noise (S/N) and/or improved spatial resolution afforded by the high-field, major improvements, compared to 3 T for example, have been seen in applications such as: (1) improved tissue contrast in susceptibility-weighted imaging (Li et al., 2006; Duyn et al., 2007), and in particular the better definition of areas of iron deposition which can be early indicators of many neurodegenerative diseases, (2) higher resolution magnetic resonance angiography with superior background tissue suppression due to the higher T_1 value of brain tissue (Maderwald et al., 2008; Zwanenburg et al., 2008; Monninghoff et al., 2009; Kang et al., 2009), (3) improved localized spectroscopy due to higher spectral resolution, higher S/N and/or smaller voxel dimensions (Tkac et al., 2001), and (4) higher resolution and sensitivity in functional MRI due to enhanced blood oxygen level dependent (BOLD) contrast (Yacoub et al., 2001), allowing differentiation of activation in separate cortical layers. Examples of each of these applications are shown in Figure 1. Many groups have also shown the clinically related advantages of high-field neurological MRI with examples in the areas of MS and cancer (Lupo et al., 2009).

The clinical promise of high-field neurological MR has already begun to be exploited in patient studies. However, there are significant engineering challenges, outlined in the next section, that have to be addressed to obtain data which takes full advantage of the high field.

II. TECHNICAL ISSUES IN HIGH-FIELD MR NEUROIMAGING

The strength of the signal received in a coil from tissue at a location r and time t is proportional to the magnitude of the transverse component of the net nuclear magnetization at that location, $M_T(r,t)$, and to the magnitude of the pertinent circularly polarized component of the RF magnetic field (B_1) of the receive coil, $B_1^-(r)$. Initially, the net nuclear magnetization vector, $\mathbf{M}(r)$, is oriented parallel to the static magnetic (B_0) field so that M_T is zero, and $\mathbf{M}$ must be manipulated via application of magnetic fields $\mathbf{B}$ at the Larmor frequency, to generate a signal. The effect of the $\mathbf{B}$ fields on $\mathbf{M}$ is described by the phenomenological Bloch equation

$$\frac{d\mathbf{M}}{dt} = \gamma(\mathbf{M} \times \mathbf{B}) - \left(\frac{M_x}{T_2}\mathbf{a}_i + \frac{M_y}{T_2}\mathbf{a}_j + \frac{M_z - M_0}{T_1}\mathbf{a}_k\right) \qquad (1)$$

where T_1, T_2, and M_0 are tissue-specific properties, γ is the gyromagnetic ratio, and $\mathbf{a}_i$, $\mathbf{a}_j$, and $\mathbf{a}_k$ are unit vectors in the x-, y-, and z-

Correspondence to: Andrew Webb; e-mail: a.webb@lumc.nl

Grant sponsors: Nederlandse Organisatie voor Wetenschappelijk Onderzoek, National Institutes of Health (R01 EB000454)

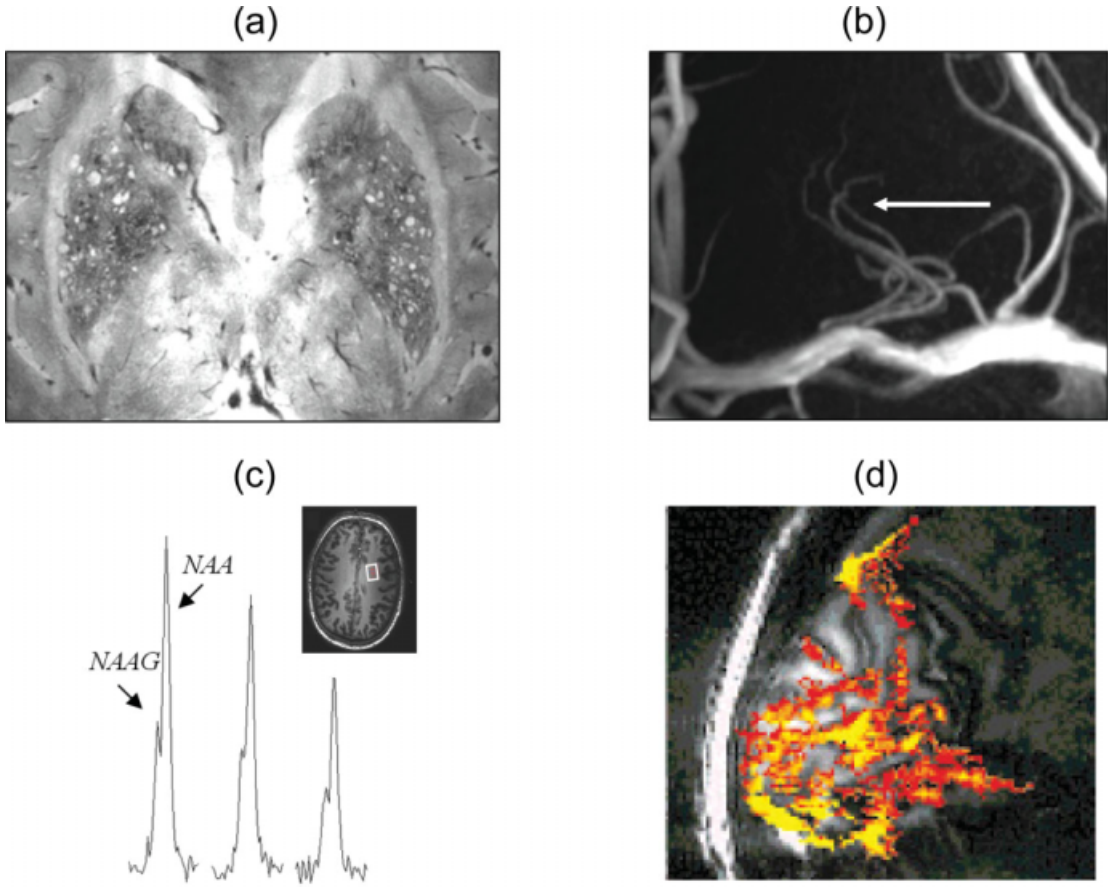

Figure 1. Four examples of neurological MR applications which are enhanced at high field. All data were acquired at 7 T. (a) Long echo time "Duyn" sequence of a patient with CADASIL. Many areas of hyperintensity associated with white matter lesions can be seen. (b) Time-of-flight angiogram showing the lenticulostriate arteries in a patient with CADASIL. Spatial resolution 230 × 230 × 230 μm^3, total data acquisition time ~10 min. (c) Diffusion-weighted spectroscopy showing separate resonance from *N*-acetylaspartate (NAA) and *N*-acetylaspartylglutamate (NAAG). Spectra are shown with *b* values of 100, 300, and 500 mm^{-2} s. (d) High-resolution functional activation map during visual stimulation (Yacoub et al., 2001); reproduced with permission from Yacoub et al., Magn Reson Med 2001, 45, 588–594, © John Wiley, Ltd. [Color figure can be viewed in the online issue, which is available at www.interscience.wiley.com.]

directions. Applying this equation in a frame of reference that rotates about the direction of B_0 (the z-axis) at the Larmor precession frequency, one can express the applied field $\mathbf{B}$ as

$$\mathbf{B}(r,t) = \mathrm{Re}\{B_1^+(r,t)\}\mathbf{a}_i + \mathrm{Im}\{B_1^+(r,t)\}\mathbf{a}_j + \left(\frac{\Delta\omega(t)}{\gamma}\right)\mathbf{a}_k + G(r,t)\mathbf{a}_k \quad (2)$$

where Re and Im represent the real and imaginary parts, respectively, of the complex amplitude of the pertinent circularly polarized component of the B_1 field produced by the transmit coil or array ($B_1^+(r,t)$), $\Delta\omega$ is the difference between the frequencies of nuclear precession and the applied B_1 field, and G is the local magnetic field created by applied gradient fields.

It is B_1^+ that initially causes $\mathbf{M}$ to tip away from the z-axis so that signal can be detected. Ideally, the magnitude of B_1^+ is homogeneous throughout the region of interest (ROI), so that the signal intensity of the reconstructed image is a function of tissue properties rather than the applied B_1 field distribution. Unfortunately, creating a homogeneous B_1^+ within tissue at higher RF frequencies is challenging due primarily to the short electromagnetic wavelength (λ). The high-relative permittivity (ε_r) of most tissues results in much shorter wavelengths in the brain than in air, for example, since the wavelength is, to first order, inversely proportional to the square root of the permittivity. The value of ε_r for brain is about 45 at 300 MHz.

Conventional volume coils used for excitation, such as a quadrature birdcage coil (Hayes et al., 1985) or transverse electromagnetic mode (TEM) resonator (Vaughan et al., 1994), are designed to produce homogeneous B_1^+ distributions at low frequencies (long wavelengths), and typically have electrical currents with equal magnitude flowing in opposite directions on opposite sides of the sample. In a symmetric sample, this can create a standing wave pattern with constructive interference near the center of the sample and with regions of destructive interference approximately one quarter wavelength away. At lower frequencies, for example, <130 MHz for 1.5 and 3 T, λ is relatively long compared to the dimensions of the brain, and so these regions of destructive interference lie outside the imaging volume and thus are of little concern. At 300 MHz (7 T), however, λ in brain is only ~13 cm, and regions of constructive and destructive interference can therefore occur.

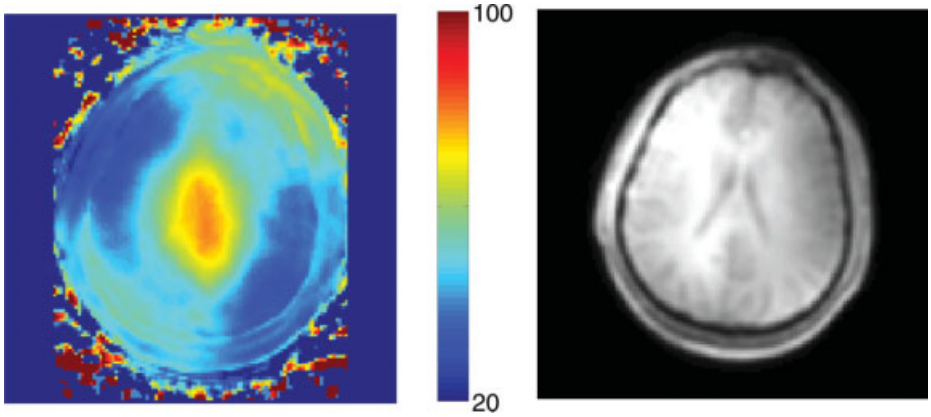

Figure 2. Left: Calculated B_1^+ map in the brain of a volunteer acquired at 7 T using a quadrature birdcage coil. Right: The corresponding low-spatial resolution axial image. The color bar represents percentage of the maximum B_1^+ field.

The second factor that affects the distribution of the B_1^+ field is the tissue conductivity (σ). In contrast to the effects of the sample's electric permittivity, σ introduces an effective ''skin-depth'' term, and damps the standing wave phenomenon. At 300 MHz, the skin depth of brain tissue is ~7.5 cm, compared to ~14.6 cm at 64 MHz. Although this effect can be considered to reduce the fields from any given current element in a coil, constructive interference from fields propagating from elements all around the head still results in an overall central brightening, sometimes described in terms of ''field focusing.'' At field strengths of 4 T and above, significant signal variation is seen across the brain in images acquired with volume coils.

Figure 2 shows a measured B_1^+ map from the head of a volunteer at 7 T using a quadrature birdcage transmit coil. The strongest field is present at the centre of the brain, and areas of low-signal intensity are evident close to the surface of the brain. The asymmetric excitation pattern, with respect to both horizontal and vertical axes, is also very clear.

For low tip-angle gradient echo images the effect of B_1^+ inhomogeneities is detrimental but not critical; however, the effect is particularly pronounced for spin-echo sequences, as shown in Figure 3. The reduced value of B_1^+ is noticeable not only in the much lower signal intensities in certain areas but also in the fact that these areas show a much reduced gray–white matter contrast due to the lower tip angle experienced. These effects make image quantitation, and image segmentation, to name but two examples, extremely difficult.

The image signal intensity (I) is a function of the transmit and receive sensitivities, and for a simple gradient echo sequence with long repetition time is proportional to the product of the sine of the transmitted tip angle multiplied by the receive sensitivity:

$$I \propto \sin(\gamma \mathbf{B}_1^+ \tau)(\mathbf{B}_1^-)^* \quad (3)$$

where τ is the duration of the RF pulse. In the low tip-angle limit, the signal is proportional to the product of transmit and receive sensitivities:

$$I \propto (\mathbf{B}_1^+)(\mathbf{B}_1^-)^* \quad (4)$$

The effect of the B_1 inhomogeneity as a function of field strength has been studied extensively (Collins and Smith, 2001; Collins et al., 2002, 2005; Wang et al., 2002; Yang et al., 2002). Figure 4 shows that even using a low tip-angle gradient echo imaging sequence, there are significant image nonuniformities at fields higher than ~4 T.

The fact that the interaction of high-frequency magnetic fields with the human body would give rise to sample-induced spatial variations in the image intensity was recognized very early in the development of MRI (Bottomley et al., 1978). Borrowing from other fields of electromagnetic-based imaging and therapy, various

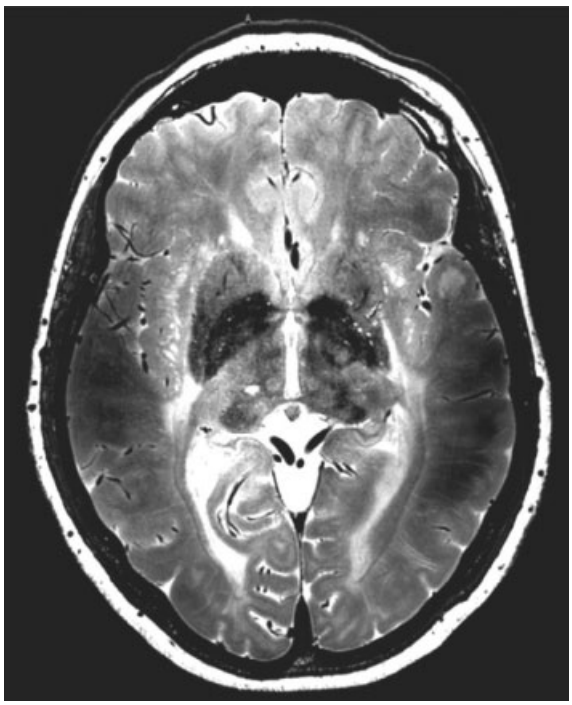

Figure 3. Low-resolution turbo spin-echo image of a volunteer acquired at 7 T using a quadrature birdcage excitation and 16-channel phased array receive. The lower signal intensity and, in particular, the lower gray–white matter contrast close to the temporal lobes indicate the intrinsically lower B_1^+ field in these areas.

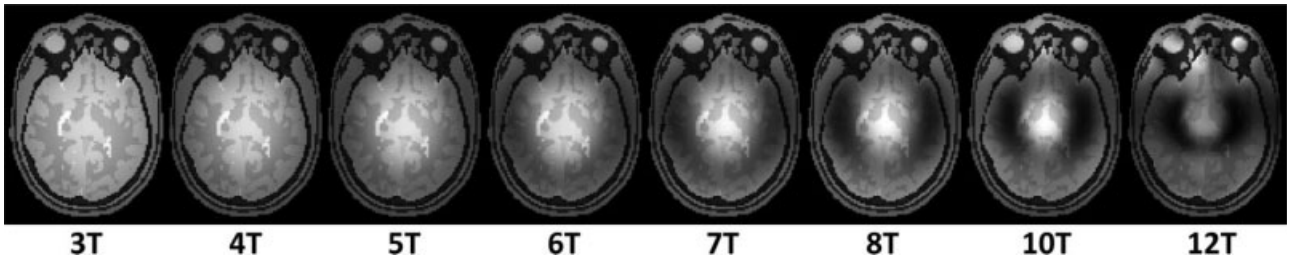

Figure 4. Simulated gradient-echo images as a function of field strength using a birdcage coil with ideal current distributions in the rungs. The signal is calculated as the product of the transmit and receive fields, assuming a low tip-angle excitation.

techniques for mitigating this phenomenon have been developed for high-field MRI and are outlined in the following sections.

III. DEVELOPMENT OF THE TRANSMIT ARRAY CONCEPT FOR ELECTROMAGNETIC HYPERTHERMIA IN HUMANS

The challenges of delivering electromagnetic energy into the human body at frequencies where the body dimensions are larger than the wavelength have been studied for a very long time, specifically in the area of electromagnetic or radiofrequency hyperthermia. Apart from the fundamental difference that hyperthermia aims to control the electric fields to produce localized therapeutic heating, the essential approach to ''guiding'' the distribution of RF energy is the same as that which has been adopted for high-field MRI, namely the use of an array of single-element, electrically decoupled applicators which are fed from separate sources. The spatial distribution of the electric field, and therefore the heating pattern within the patient can be controlled by varying the phase and magnitude of the RF supplied to each element of the array from individual amplifiers (Sullivan, 1991; Wust et al., 1991; Kowalski and Jin, 2000, 2003a,b, 2004; Kowalski et al., 2002; Behnia et al., 2002, 2004; Weihrauch et al., 2007). An example of a modern, commercial multi-element array used for patient hyperthermia is shown in Figure 5. Also shown in Figure 5 are illustrations of the way in which the focal point of the electric fields can be steered by changing the phase of each of the dipole elements.

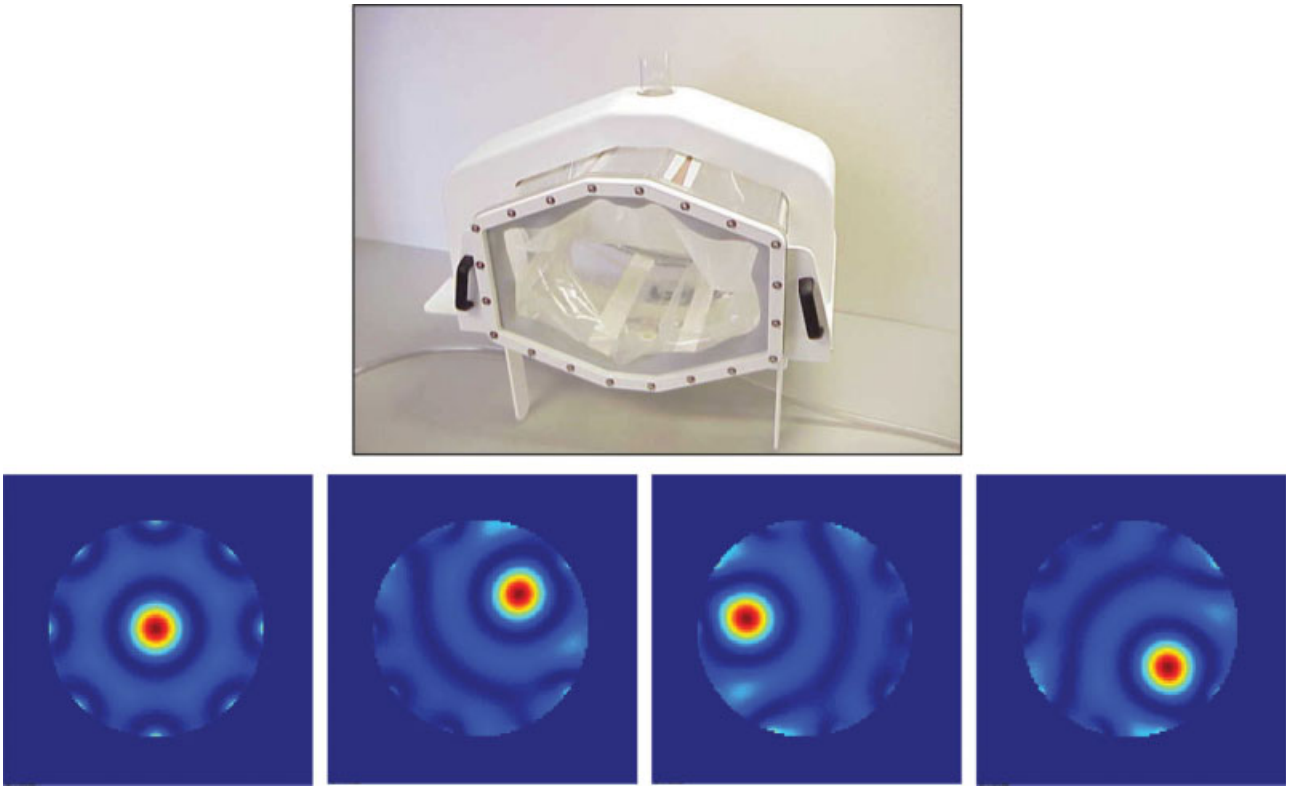

Figure 5. Upper: A commercial six-element electric dipole hyperthermia applicator, in which the magnitude and phase of the input signal can be changed. Bottom: Different heating patterns that can be produced using "shimming" of the electric fields. An eight-element dipole array is used, with different phases (but equal magnitudes) applied to each dipole. With all phases equal, the electric fields are "focused" in the center of the phantom (bottom left). By varying the phase, the location of the focus can be moved around, as shown by the figures to the right. The sample is a uniform sphere with dielectric constant of 80. The greater the number of elements in the array, the tighter the focus, and the greater the ability to steer the focus. [Color figure can be viewed in the online issue, which is available at www.interscience.wiley.com.]

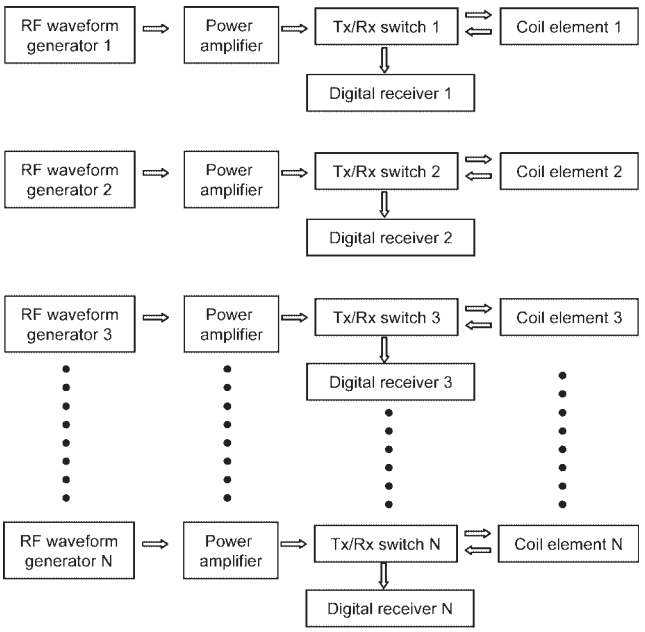

Figure 6. Schematic of the hardware required to implement an N-element transmit array with variable magnitude and phase of the input signal to each element of the array. There are a number of less expensive but more limited variations in which the RF signals may be provided from a single waveform generator and then fed to each channel using a power-splitter.

IV. TRANSMIT ARRAYS FOR HIGH-FIELD MRI

In principle, an RF system for high-field MRI in which the magnitude and phase of the current in conductive elements about the head are controlled individually (rather than having equal and opposite values on opposite sides of the subject and thus creating a strong standing wave pattern) should be able to produce much more homogeneous fields than a conventional volume coil at high frequencies. As outlined earlier, the idea behind transmit arrays is to have control of the magnitude and phase of the RF supplied to each element of the array and, based either on measurements or simulations, to optimize the signal input to each element of the RF coil to improve the excitation homogeneity, minimize tissue heating, or a combination of the two.

A. Required System Hardware. A wide variety of approaches have been used to realize transmit arrays for MRI. The most simple manifestations use the output from a single high-power RF amplifier, which is split into numerous individual channels via a power splitter (van de Moortele et al., 2005). Each of the RF outputs (channels) passes through a controllable phase shifter and attenuator, based on a vector modulator or similar circuit. Each channel is then fed into individual transmit–receive (T/R) switches. Typically, measurement of the B_1^+ transmit field is performed, and either closed-loop or open-loop feedback control is used to iteratively adjust the phase and/or magnitude of each channel to fulfill the particular B_1 target goal (Metzger et al., 2008). More recent implementations have individual waveform generators and RF amplifiers for each channel, which allows different RF waveforms to be sent to each element of the transmit array: a schematic of such an arrangement is shown in Figure 6.

If there is the capability to interact on a real-time basis with the system hardware, then variations in the magnitude and phase of each transmit channel can be controlled by suitable changes in the waveform fed to each channel. If this is not possible, then external vector-modulator control of the phase and magnitude can be implemented, and the inputs to these components then form part of the feedback loop.

B. Transmit Array Coils: Stripline and Loop Arrays. A variety of different coil geometries can be used for a transmit array: the two most common are the shielded loop and stripline designs shown in Figure 7 (Adriany et al., 2005, 2008; van de Moortele et al., 2005). The stripline has found most use due to ease of construction, higher B_1 field close to the individual elements, and ease of element decoupling. In the stripline coil shown in Figure 7, the dielectric used is 5-mm-thick PTFE with a permittivity of 2.1 (Adriany et al., 2005). The width of each stripline (12 mm) was chosen according to standard microstrip design formulae to achieve an input impedance close to 50 Ω: 20-mm-wide copper tape was used for the outside ground conductor. The stripline elements can either be decoupled by a calculated geometrical element arrangement (in terms of substrate thickness, conductor width, and element separation) (Lee et al., 2001, 2004), or by the addition of a capacitive decoupling network (Zhang and Webb, 2004). Finally, each element is fine-tuned to be impedance matched to exactly 50 Ω and connected to a separate transmit–receive switch.

C. Experimental Results Using Transmit Arrays. Figure 8 shows the transmit and receive field sensitivities obtained from a uniform phantom using the eight-element stripline coil shown in Figure 7 (van de Moortele et al., 2005). As expected (Collins et al., 2002), the transmit and receive fields are very close to being mirror images of one another about a plane of relative symmetry passing through the centers of the active coil and the sample. The images also show spatial differences between the maxima of the respective fields. The excellent degree of decoupling between the elements of the stripline array is also apparent from the results.

In vivo results, shown in Figure 9, obtained at 9.4 T using a similar stripline array illustrate the increase in signal homogeneity that is achievable simply by changing the phase of two elements of the array, in this case, the two elements closest to the area in which the B_1 field is most inhomogeneous (Vaughan et al., 2006).

The limits of RF shimming have been investigated theoretically using numerical calculations by Mao et al. (2006). They found that a 16-element array can effectively shim a single slice at frequencies up to 600 MHz (14.1 T) and the whole brain at frequencies up to 300 MHz, whereas an 80-element array can shim the whole brain up to 600 MHz.

D. Transmit Arrays Using Active Rungs. A recently proposed alternative approach to transmit array implementation involves the use of an active electronic device such as a transistor integrated with each element of the array: each rung is termed an ''active rung'' (Kurpad et al., 2006; Lee et al., 2009). The use of an active device such as a bipolar-junction transistor (BJT) or metal-oxide-semiconductor field-effect transistor (MOSFET) to drive integrated antenna elements has been shown to make the feed network of antenna arrays less sensitive to the effects of mutual impedance than passive arrays because of the unidirectional nature of the active devices (Chang et al., 2002). This approach maintains the ability to provide independent control of the magnitude and phase of the

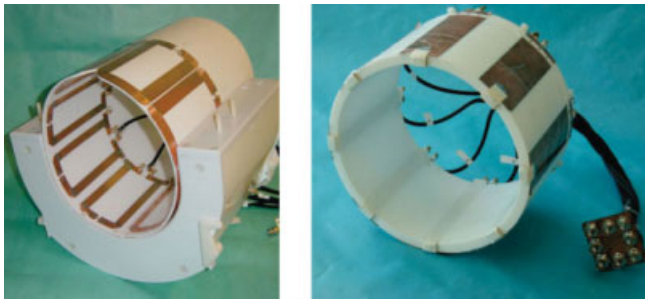

Figure 7. Examples of shielded loop (left) and stripline (right) transmit arrays constructed for neurological applications at 7 T Adriany et al., Magn Reson Med 2005;53:434-445, copyright John Wiley, Ltd. [Color figure can be viewed in the online issue, which is available at www.interscience.wiley.com.]

driving voltage to each element of the array, and also has excellent isolation between separate array elements. Use of a power MOSFET with output power up to 1 kW and decoupling between nearest neighbors of close to 20 dB has recently been reported for a two-element array operating at 3 T (Lee et al., 2009). A schematic of the electronic circuit is shown in Figure 10.

E. Advanced RF Pulse Design for Use with Transmit Arrays. As outlined previously, there is a limit to the B_1^+ inhomogeneity mitigation that can be achieved using transmit arrays alone, unless a very large number of elements are available. An alternative method to make improvements is to implement RF pulses, which themselves inherently compensate for B_1^+ inhomogeneities. These general ideas are very familiar from high-resolution NMR spectroscopy, which has a rich history in the design of such RF pulses (Levitt, 1986).

Considering Eq. (1), by targeting a homogeneous M_T distribution after a series of two RF pulses, rather than aiming for a homogeneous B_1^+ distribution for either of the individual pulses, Collins et al. (2007) were able to optimize the magnitudes and phases for each pulse for each of the elements in a 16-channel array to achieve significant improvements in excitation homogeneity compared to an RF shimming approach with a single RF pulse, and the results are shown in Figure 11.

As seen in Eq. (2), it should be possible in some cases to compensate for inhomogeneity in B_1^+ with strategic use of a time-dependent offset frequency ($\Delta\omega$) or gradient field distribution (G). Examples of how this can be accomplished with a single coil are seen in the use of adiabatic pulses (using $\Delta\omega$) (Tannus and Garwood, 1997) and in tailored RF pulses (using G) (Pauly et al., 1989). Using concepts related to parallel reception, it is also possible to use a transmit array to accelerate tailored RF pulses (Katscher et al., 2003). This allows for excitation patterns that are seemingly limited more by the user's imagination than by the bounds of the Maxwell equations (Setsompop et al., 2006).

Another idea using gradients and transmit arrays uses k-space ''spokes'' (Saekho et al., 2005, 2006) to mitigate B_1^+ inhomogeneity. Three-dimensional RF pulses are used, which consist of modulated sinc-like pulse segments (spokes) in the k_z direction of excitation k-space positioned at predetermined locations in (k_x, k_y). Spoke-based pulses are used in the small-tip-angle regime, in which the sinc-like RF segments in k_z produce slice-selectivity in z, and the amplitude and phase modulation of each spoke in (k_x, k_y) spatially tailors the excitation in (x, y) to mitigate the in-plane inhomogeneity. An ideal B_1^+ mitigation pulse excites the point-wise inverse of the inhomogeneity and yields a uniform magnetization. This approach has also recently been integrated with multiple-element transmit arrays (Zelinski et al., 2008; Setsompop et al., 2009) with significant improvements in image uniformity.

V. SPECIFIC ABSORPTION RATE AND TEMPERATURE CONSIDERATIONS

Associated with any RF magnetic field is a corresponding RF electric field, which produces electrical currents in conductive tissues. A key consideration in assessing the practical viability of any transmit array and/or associated imaging sequence is the power deposition in tissue, quantified via the local and average specific absorption rate (SAR) values, measured in Watts per kilogram of tissue.

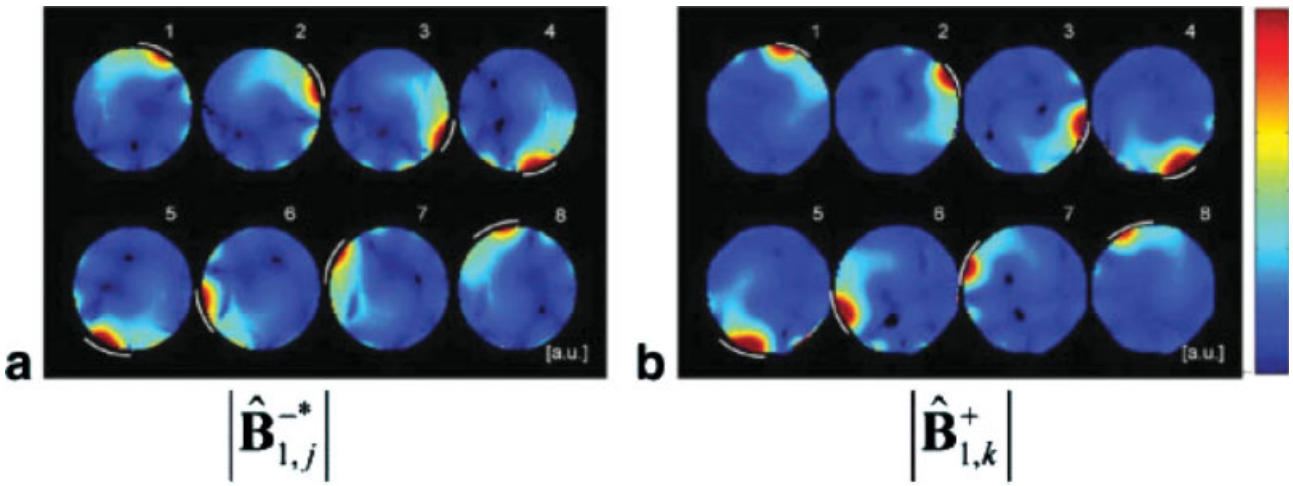

Figure 8. Individual coil element B_1 mapping from a uniform phantom using an eight-element stripline coil. (a) Individual coil element receive B_1 maps (derived from one data set obtained by transmitting through all coil elements). (b) Individual coil element transmit B_1 maps derived from eight experiments transmitting through one coil element at a time. Figure reproduced with permission from van de Moortele et al., Magn Reson Med 2005;54:1503–1518, © John Wiley, Ltd.

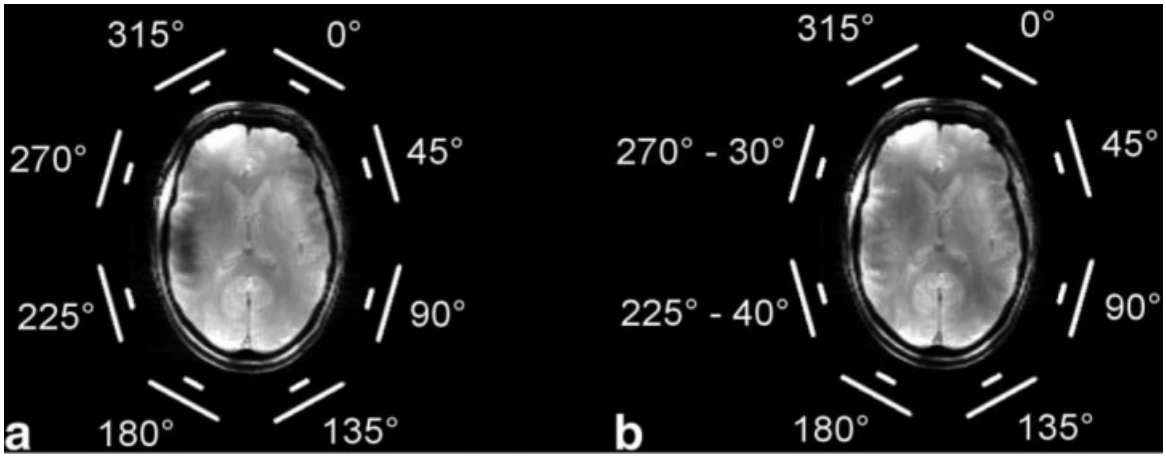

Figure 9. Effect of the transmit phase on image homogeneity at 9.4 T. (a) Scout FLASH image of a head inside a circularly polarized elliptical coil. The loss of signal near the left ear is the result of destructive interference reducing the net B_1^+. The relative transmit phase for each coil labeled near the two lines representing the conductor and ground planes of each coil is shown. (b) By adjusting only the relative transmit phase of the two coils closest to the area of low-signal intensity, local destructive interference can be reduced. Figure reproduced with permission from Vaughan et al., Magn Reson Med 2006;56:1274–1282, © John Wiley, Ltd.

There are strict regulatory guidelines on these values (IEC, 2002) in terms of peak instantaneous and time-averaged values for both local and global ROI. With the emergence of transmit array technologies, where it is possible to have a very wide range of maximum local SAR for a given patient, array configuration, and average SAR value, numerical methods to rapidly and accurately predict SAR distributions using sophisticated models of heterogeneous human anatomies have played an increasingly important role in RF coil and sequence development and assessment (Collins et al., 2004; Wang et al., 2007). The SAR can be calculated from the electric field (E) distributions which are estimated from, for example, full-Maxwell calculations of the electromagnetic fields using finite difference time domain techniques, and is given by:

$$\mathrm{SAR} = \frac{\sigma}{2\rho}|\mathrm{E}|^2 \tag{5}$$

where ρ is the material density. An equally important measure is the temperature (T) in the head, which can be modeled with a finite difference implementation of the Pennes bioheat equation (Pennes, 1948):

$$\rho c\frac{dT}{dt} = \nabla\cdot(k\nabla T) + [-\rho_{\mathrm{blood}} w c_{\mathrm{blood}}(T - T_{\mathrm{core}})] + Q_{\mathrm{m}} + \mathrm{SAR}_{\rho} \tag{6}$$

where c is the tissue heat capacity; k, the thermal conductivity; w, the blood perfusion; and Q_{m} the heat generated by metabolism.

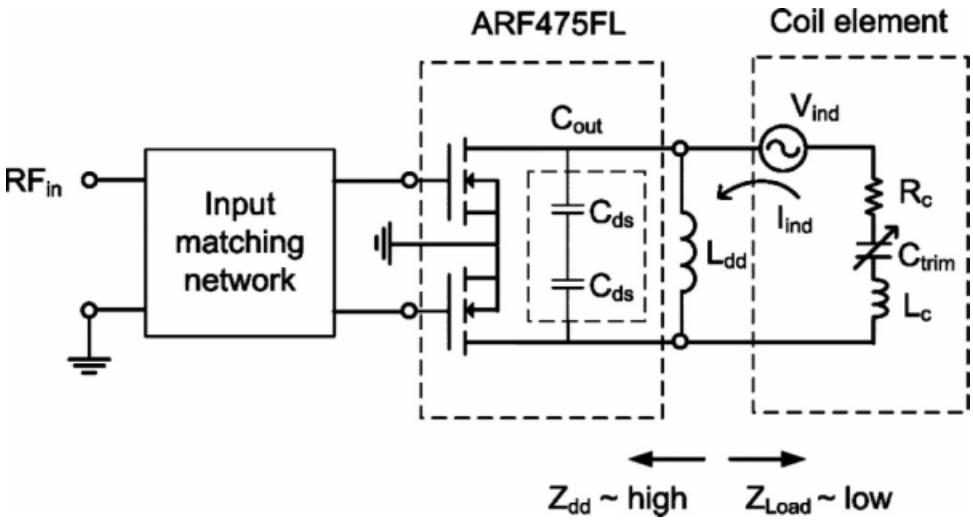

Figure 10. Schematic circuit of a controlled RF current source (RFCS) using an ARF475FL RF power MOSFET operated in push–pull mode. The output circuit consisted of a series-tuned driven loop (11-cm diameter) across the drain-to-drain terminal. A high-output impedance (Z_{dd}) looking into the drain-to-drain is formed by the parallel tank circuit (L_{dd} and C_{out}). An input-matching network drives balanced RF signals into the symmetrical gate terminals with a gate-stabilizing circuit. The matching circuit also transforms the low-gate impedance to the 50 Ω feed input of the current source for maximum transfer of the input driving power. Figure reproduced with permission from Lee et al., Magn Reson Med, 2009, 62, 218–228, © John Wiley, Ltd.

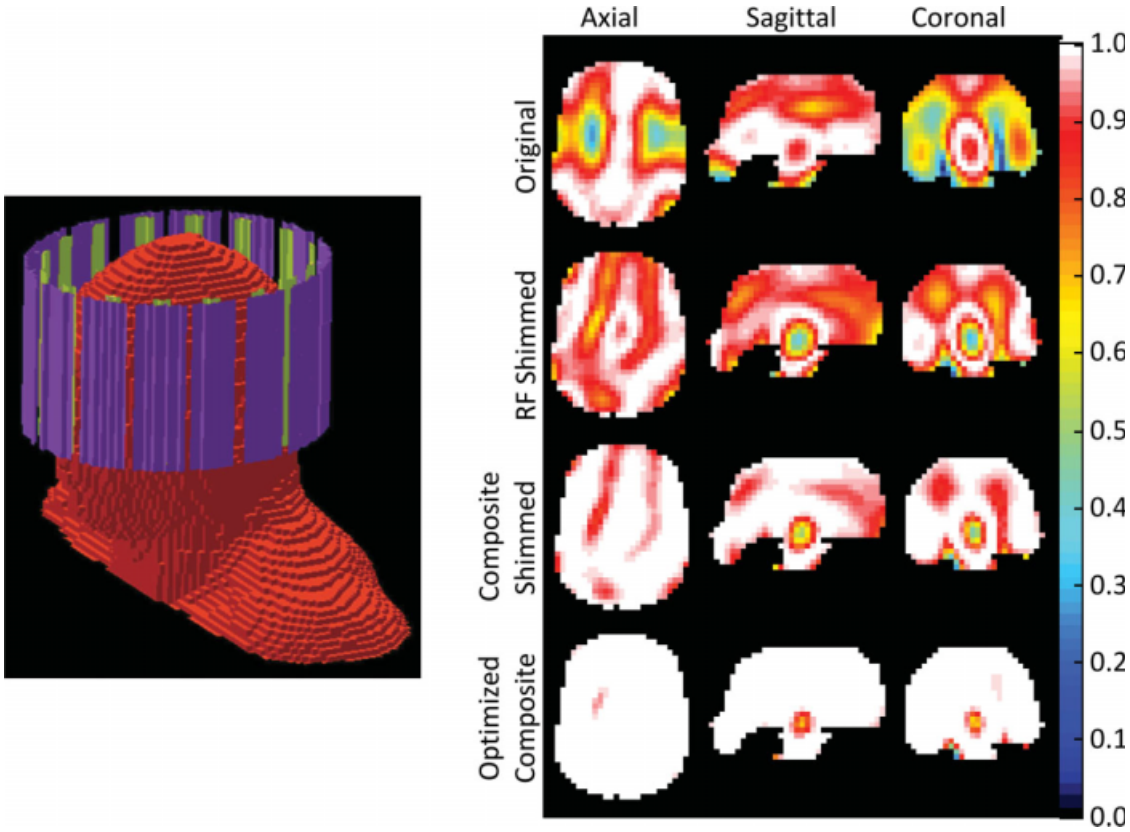

Figure 11. Left: Shaded-surface rendition of the 3D digital head model and 16-element coil array used in numerical simulations. Right: The 16-element optimization of gradient echo signal intensity maps of single slices and whole brain at 300 MHz. From top to bottom: standard drive before optimization, optimization on an axial slice, optimization on a sagittal slice, optimization on a coronal slice, optimization on the whole brain. Three orthogonal views (from left-to-right: axial slice, sagittal slice, and coronal slice) are shown for each driving condition. Figure reproduced with permission from Collins et al., Magn Reson Med 2007;57:470–474, © John Wiley, Ltd.

Figure 12 illustrates the SAR distribution in the brain at 3 and 7 T, showing very different heating patterns at the two different frequencies (Collins et al., 2004).

VI. RECEIVE ARRAY TECHNOLOGY

The use of receive arrays on clinical MRI systems has become universal over the past decade. In research laboratories, 32 (Wiggins et al., 2006) and 96 (Wiggins et al., 2009) channel receive array coils have been demonstrated at 3 T for neurological applications, and commercial systems exist for 32 and 16 channels at 7 T. As with transmit arrays, individual receive elements must be electrically decoupled from one another. This is much simpler for receive arrays since, in addition to optimal overlap to reduce mutual inductance, impedance mismatched preamplifiers can be used to reduce the current in each coil element and therefore increase the intercoil decoupling (Roemer et al., 1990). Essentially, the original concepts introduced by Roemer et al. (1990) and Wright et al. (1991) form the basis of all receive arrays currently in use. Additionally, each element must also be decoupled from each element of the transmit array or transmit volume coil, and this is achieved using active PIN diode switching circuits. Providing that the individual elements of the array are sufficiently large such that body noise is the dominant noise source, then the signal intensity from a large phased array is significantly higher than that from an equivalently sized volume resonator, as shown in Figure 13.

Since receive coils are not actively creating fields, if they are adequately decoupled from each other then their sensitivity patterns are fairly independent. The effects of a receive array on the signal intensity distribution in the final image are, therefore, very different from those of a transmit array, since no vector summation of fields from different elements or associated interference effects occur, and standing wave patterns do not form.

Receive arrays are primarily used for parallel imaging, in which a reduced number of phase encoding steps is traded-off for a (spatially dependent) loss in signal-to-noise. The more sparse *k*-space coverage enables faster imaging, and also reduces artifacts in single-shot imaging techniques such as echo planar imaging. The basic principle of parallel imaging is that the different weighting of the signal at a given location from different receive coils can be used, in part, to determine the spatial origin of the signal, lessening the need for time-consuming gradient encoding. Parallel imaging techniques can be broadly categorized as working primarily in the image domain or in the k-space domain (Sodickson and McKenzie, 2001). There are a few commonly used techniques, and a plethora of variations on the theme. In the *k*-space-based technique known as generalized autocalibrating partially parallel acquisitions (GRAPPA) (Griswold et al., 2002), lines in *k*-space are skipped at regular

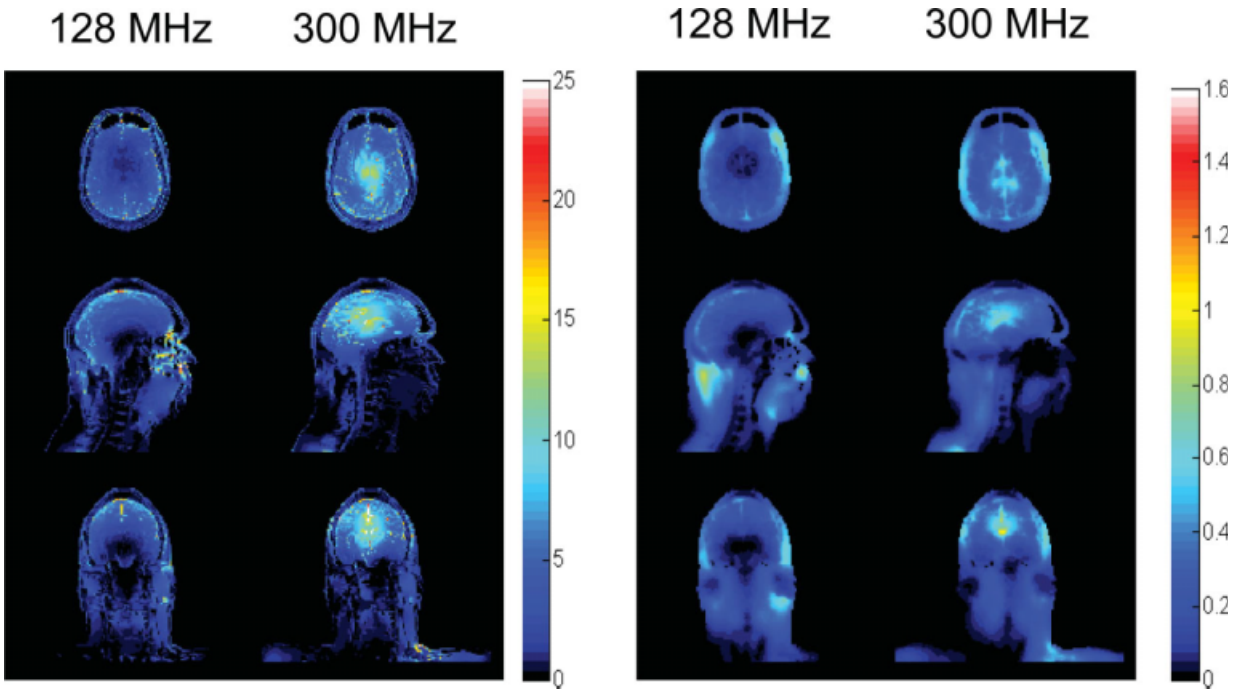

Figure 12. Calculated distributions of (left) SAR (W/kg) and (right) corresponding temperature increase (°C) at 3 T (128 MHz) and 7 T (300 MHz) modeled during exposure to a head-average SAR of 3.0 W/kg. (Top) An axial plane passing through the center of the coil and brain, (center) corresponding sagittal and (bottom) coronal planes. The simulated RF coil was a 16-element TEM resonator with rung currents equal in magnitude and with a phase given by their azimuthal position.

intervals during the acquisition process, but a few of these lines, termed autocalibration scan (ACS) lines, are acquired in a reference scan. Numerical functions for fitting the data from the acquired lines of *k*-space from multiple coils to the ACS lines in the data from each coil are determined, and these functions are applied to synthesize all the missing lines of *k*-space in the data from all coils. One of the main advantages of GRAPPA is that it requires no measurement of the receptivity (B_1^-) distribution from the receive coils.

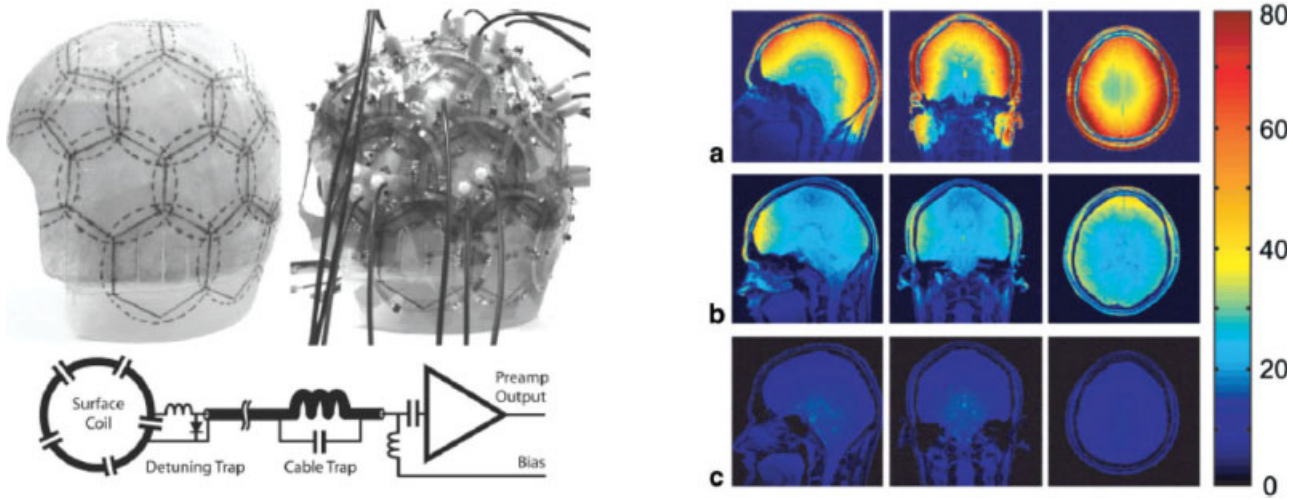

Figure 13. Top left: Fiberglass helmet with hexagonal and pentagonal tiling pattern (solid lines) and approximate circular coil positions (dotted lines) drawn on to the helmet. Top right: Completed helmet with surface coils and cables attached. Bottom: Circuit schematic for the surface coil and preamp chain, showing the diode detuning trap at the coil, cable trap for common mode rejection (located on preamp circuit board), bias T, and preamplifier. Right: SNR maps derived from gradient-echo scans for (a) a 32-channel coil, (b) a commercial eight-channel coil, and (c) a commercial CP volume coil. All maps are generated with the same color scale for comparison. Figure reproduced with permission from Wiggins et al., Magn Reson Med 2006;56:216–223, © John Wiley, Ltd.

An alternative, image-based, parallel imaging strategy is the sensitivity encoding (SENSE) method (Pruessmann et al., 1999). This method provides an optimized reconstruction, with no weighting of the signal by the coil receptivity distributions in the final image if a perfectly accurate complex coil sensitivity map can be obtained. If the acquired *k*-space data are reduced by a factor of *R* by skipping certain *k*-space lines, inverse Fourier transformation of the data from all the coils in the array leads to aliased images. To reconstruct an accurate image of the sample, the true signals and aliased signals have to be separated. This can be achieved since, in the image from each individual coil, signal superposition occurs with different weights according to the local coil sensitivities. The unaliased components, *v*, of every aliased pixel can be obtained by an appropriate linear combination of the pixel values in the various single-coil images:

$$v = (S^{H}\Psi^{-1}S)^{-1}S^{H}\Psi^{-1}a \qquad (7)$$

where vector *v* contains the unaliased pixel values; *a*, the aliased values; *S*, the complex coil sensitivities (the superscript H represents the transposed complex conjugate); and Ψ represents noise correlation in the receiver channels. As seen in Figure 14, SENSE can effectively remove the weighting of the receive coil field distributions from the final image (Sodickson and McKenzie, 2001). In these cases, the S/N distribution, however, will typically not be uniform throughout the image (Pruessmann et al., 1999), and these methods usually require mapping of the complex B_1^- distribution of each coil, which is not straightforward at high frequencies (van de Moortele et al., 2005).

Generally, the larger the number of receive coils, the higher the acceleration factor (*R*) that can be used to reconstruct the images, the more sparse the *k*-space coverage and the larger the reduction in data acquisition time. However, associated with reduced *k*-space coverage is a noise amplification, or *g*-factor (Pruessmann et al., 1999). The *g*-factor is not uniform throughout the image, and increases rapidly as a function of *R*. However, the *g*-factor also decreases the larger the number of receive channels, and this reduction is in general the driving factor behind the large and increasing number of channels being produced both commercially and academically. Figure 15 shows the interaction between *g*-factor, number of coils and acceleration factor from data from Wiggens et al. (2006, 2009).

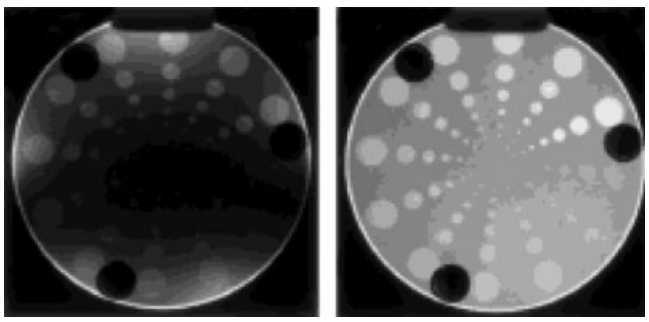

Figure 14. Two different receive array reconstruction methods yield very different images. A SENSE reconstruction (right) can effectively remove intensity weighting due the field pattern of the receive coils clearly evident in a sum-of-squares reconstruction (left). Figure reproduced from Pruessmann et al., Magn Reson Med 1999;42:952–962, with permission from John Wiley, Ltd.

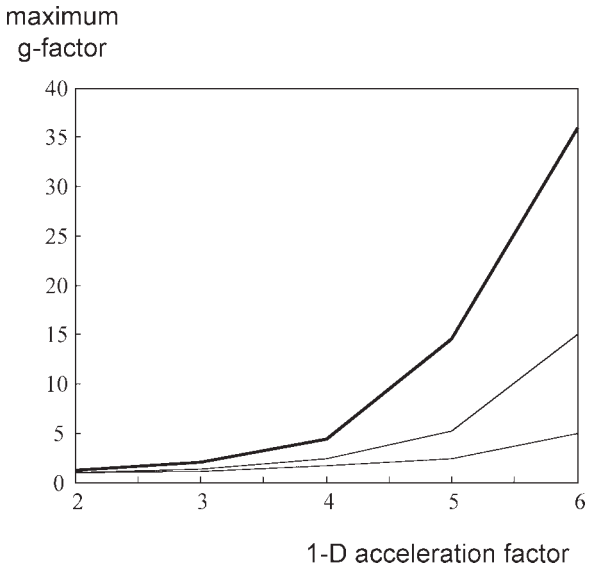

Figure 15. Plot of the maximum *g*-factor versus 1D acceleration factor for three different receive array coils containing 96 elements (dotted line), 32 elements (thin solid line), and 8 elements (thick solid line). Each coil was designed for neuroimaging at 3 T.

It is also worth noting that the increased sample-induced inhomogeneity in the magnitude and phase of the image, which occurs at higher field does have a potential advantage, in that this results in a decrease in the *g*-factor as a function of frequency for a given receive array geometry (Wiesinger et al., 2004a,b, 2006).

VII. CONCLUSIONS

Clinical MR neuroimaging at 7 T and above has already resulted in many applications in which the diagnostic quality is significantly greater than at 3 T, and a number of patient studies are currently being performed worldwide. Many imaging protocols, however, remain challenging due to B_1 inhomogeneity and SAR deposition, as well as B_0 effects (which have not been discussed in this article). Engineering solutions, such as the development of transmit arrays, receive arrays and optimized RF pulse design, have the potential to overcome almost all of these challenges at 7 T, and to make substantial improvements in image quality at even higher fields (9.4 and 11.7 T) that are at the forefront of current MRI technology.

ACKNOWLEDGMENTS

Figures were kindly provided by Drs. Thomas Vaughan, Pierre-Francois van der Moortele, Zhangwei Wang, and Gregor Adriany.

REFERENCES

G. Adriany, P.F. van de Moortele, F. Wiesinger, S. Moeller, J.P. Strupp, P. Andersen, C. Snyder, X. Zhang, W. Chen, K.P. Pruessmann, P. Boesiger, T. Vaughan, and K. Ugurbil, Transmit and receive transmission line arrays for 7 Tesla parallel imaging, Magn Reson Med 53 (2005), 434–445.

G. Adriany, P.F. van de Moortele, J. Ritter, S. Moeller, E.J. Auerbach, C. Akgun, C.J. Snyder, T. Vaughan, and K. Ugurbil, A geometrically adjustable 16-channel transmit/receive transmission line array for improved RF efficiency and parallel imaging performance at 7 Tesla, Magn Reson Med 59 (2008), 590–597.

B. Behnia and A.G. Webb, MRI-monitored electromagnetic heating using iterative feedback control and phase interference mapping, Conc Magn Reson B 23 (2004), 1–15.

B. Behnia, M. Suthar, and A.G. Webb, Closed-loop feedback control of phased-array microwave heating using thermal measurements from magnetic resonance imaging, Conc Magn Reson B 15 (2002), 101–110.

P.A. Bottomley and E.R. Andrew, RF magnetic field penetration, phase shift and power dissipation in biological tissue: Implications for NMR imaging, Phys Med Biol 23 (1978), 630–643.

K. Chang, R.A. York, P.S. Hall, and T. Itoh, Active integrated antennas, IEEE Trans Microwave Theory Tech 50 (2002), 937–944.

C.M. Collins and M.B. Smith, Calculations of B1 distribution, SNR, and SAR for a surface coil adjacent to an anatomically-accurate human body model, Magn Reson Med 45 (2001), 692–699.

C.M. Collins, Q.X. Yang, J.H. Wang, X. Zhang, H. Liu, S. Michaeli, X.H. Zhu, G. Adriany, J.T. Vaughan, P. Anderson, H. Merkle, K. Ugurbil, M.B. Smith, and W. Chen, Different excitation and reception distributions with a single-loop transmit-receive surface coil near a head-sized spherical phantom at 300 MHz, Magn Reson Med 47 (2002), 1026–1028.

C.M. Collins, W. Liu, J. Wang, R. Gruetter, J.T. Vaughan, K. Ugurbil, and M.B. Smith, Temperature and SAR calculations for a human head within volume and surface coils at 64 and 300 MHz, J Magn Reson Imaging 19 (2004), 650–656.

C.M. Collins, W. Liu, W. Schreiber, Q.X. Yang, and M.B. Smith, Central brightening due to constructive interference with, without, and despite dielectric resonance, J Magn Reson Imaging 21 (2005), 192–196.

C.M. Collins, Z.W. Wang, W.H. Mao, J.M. Fang, W.Z. Liu, and M.B. Smith, Array-optimized composite pulse for excellent whole-brain homogeneity in high-field MRI, Magn Reson Med 57 (2007), 470–474.

J.H. Duyn, G.P. van, T.Q. Li, J.A. de Zwart, A.P. Koretsky, and M. Fukunaga, High-field MRI of brain cortical substructure based on signal phase, Proc Natl Acad Sci USA 104 (2007), 11796–11801.

M.A. Griswold, P.M. Jakob, R.M. Heidemann, M. Nittka, V. Jellus, J. Wang, B. Kiefer, and A. Haase, Generalized autocalibrating partially parallel acquisitions (GRAPPA), Magn Reson Med 47 (2002), 1202–1210.

C.E. Hayes, W.A. Edelstein, J.F. Schenck, O.M. Mueller, and M. Eash, An efficient, highly homogeneous radiofrequency coil for whole-body Nmr imaging at 1.5-T, J Magn Reson 63 (1985), 622–628.

IEC, International standard, medical equipment. II. Particular requirements for the safety of magnetic resonance equipment for medical diagnosis, 2nd revision, International Electrotechnical Commission, Geneva 601-2-33 (2002).

C.K. Kang, C.W. Park, J.Y. Han, S.H. Kim, C.A. Park, K.N. Kim, S.M. Hong, Y.B. Kim, K.H. Lee, and Z.H. Cho, Imaging and analysis of lenticulostriate arteries using 7.0-Tesla magnetic resonance angiography, Magn Reson Med 61 (2009), 136–144.

U. Katscher, P. Bornert, C. Leussler, and J.S. van den Brink, Transmit SENSE, Magn Reson Med 49 (2003), 144–150.

M.E. Kowalski, B. Behnia, A.G. Webb, and H.M. Jin, Optimization of electromagnetic phased-arrays for hyperthermia via magnetic resonance temperature estimation, IEEE Trans Microwave Theory Tech 49 (2002), 1229–1241.

M.E. Kowalski and H.M. Jin, Model-order reduction of nonlinear models of electromagnetic phased-array hyperthermia, IEEE Trans Biomed Eng 50 (2003a), 1243–1254.

M.E. Kowalski and J.M. Jin, A temperature-based feedback control system for electromagnetic phased-array hyperthermia: Theory and simulation, Phys Med Biol 48 (2003b), 633–651.

M.E. Kowalski and H.M. Jin, Model-based optimization of phased arrays for electromagnetic hyperthermia, IEEE Trans Microwave Theory Tech 52 (2004), 1964–1977.

M.E. Kowalski and J.M. Jin, Determination of electromagnetic phased-array driving signals for hyperthermia based on a steady-state temperature criterion, IEEE Trans Microwave Theory Tech 48 (2000), 1864–1873.

K.N. Kurpad, S.M. Wright, and E.B. Boskamp, RF current element design for independent control of current amplitude and phase in transmit phased arrays, Conc Magn Reson B 29 (2006), 75–83.

R.F. Lee, C.J. Hardy, D.K. Sodickson, and P.A. Bottomley, Lumped-element planar strip array (LPSA) for parallel MRI, Magn Reson Med 51 (2004), 172–183.

R.F. Lee, C.R. Westgate, R.G. Weiss, D.C. Newman, and P.A. Bottomley, Planar strip array (PSA) for MRI, Magn Reson Med 45 (2001), 673–683.

W. Lee, E. Boskamp, T. Grist, and K. Kurpad, Radiofrequency current source (RFCS) drive and decoupling technique for parallel transmit arrays using a high-power metal oxide semiconductor field-effect transistor (MOSFET), Magn Reson Med 62 (2009), 218–228.

M.H. Levitt, Composite pulses, Prog NMR Spectroscopy 18 (1986), 61–122.

T.Q. Li, G.P. van, H. Merkle, L. Talagala, A.P. Koretsky, and J. Duyn, Extensive heterogeneity in white matter intensity in high-resolution T2*-weighted MRI of the human brain at 7.0 T, Neuroimage 32 (2006), 1032–1040.

J.M. Lupo, S. Banerjee, K.E. Hammond, D.A.C. Kelley, D. Xu, S.M. Chang, D.B. Vigneron, S. Majumdar, and S.J. Nelson, GRAPPA-based susceptibility-weighted imaging of normal volunteers and patients with brain tumor at 7 T, Magn Reson Imaging 27 (2009), 480–488.

S. Maderwald, S.C. Ladd, E.R. Gizewski, O. Kraff, J.M. Theysohn, K. Wicklow, C. Moenninghoff, I. Wanke, M.E. Ladd, and H.H. Quick, To TOF or not to TOF: Strategies for non-contrast-enhanced intracranial MRA at 7 T, MAGMA 21 (2008), 159–167.

W. Mao, M.B. Smith, and C.M. Collins, Exploring the limits of RF shimming for high-field MRI of the human head, Magn Reson Med 56 (2006), 918–922.

G.J. Metzger, C. Snyder, C. Akgun, T. Vaughan, K. Ugurbil, and P.F. van de Moortele, Local B1+ shimming for prostate imaging with transceiver arrays at 7T based on subject-dependent transmit phase measurements, Magn Reson Med 59 (2008), 396–409.

C. Monninghoff, S. Maderwald, J.M. Theysohn, O. Kraff, S.C. Ladd, M.E. Ladd, M. Forsting, H.H. Quick, and I. Wanke, Evaluation of intracranial aneurysms with 7 T versus 1.5 T time-of-flight MR angiography—Initial experience, Rofo 181 (2009), 16–23.

J. Pauly, D. Nishimura, and A. Macovski, A K-space analysis of small-tip-angle excitation, J Magn Reson 81 (1989), 43–56.

H.H. Pennes, Analysis of tissue and arterial blood temperatures in the resting normal human forearm, J Appl Physiol 1 (1948), 93–122.

K.P. Pruessmann, M. Weiger, M.B. Scheidegger, and P. Boesiger, SENSE: Sensitivity encoding for fast MRI, Magn Reson Med 42 (1999), 952–962.

P.B. Roemer, W.A. Edelstein, C.E. Hayes, S.P. Souza, and O.M. Mueller, The NMR phased array, Magn Reson Med 16 (1990), 192–225.

S. Saekho, C.Y. Yip, D.C. Noll, F.E. Boada, and V.A. Stenger, Fast-kz three-dimensional tailored radiofrequency pulse for reduced B1 inhomogeneity, Magn Reson Med 55 (2006), 719–724.

S. Saekho, F.E. Boada, D.C. Noll, and V.A. Stenger, Small tip angle three-dimensional tailored radiofrequency slab-select pulse for reduced B1 inhomogeneity at 3 T, Magn Reson Med 53 (2005), 479–484.

K. Setsompop, V. Alagappan, B.A. Gagoski, A. Potthast, F. Hebrank, U. Fontius, F. Schmitt, L.L. Wald, and E. Adalsteinsson, Broadband slab selection with B1+ mitigation at 7T via parallel spectral-spatial excitation, Magn Reson Med 61 (2009), 493–500.

K. Setsompop, L.L. Wald, V. Alagappan, B. Gagoski, F. Hebrank, U. Fontius, F. Schmitt, and E. Adalsteinsson, Parallel RF transmission with eight channels at 3 Tesla, Magn Reson Med 56 (2006), 1163–1171.

D.K. Sodickson and C.A. McKenzie, A generalized approach to parallel magnetic resonance imaging, Med Phys 28 (2001), 1629–1643.

D. Sullivan, Mathematical-methods for treatment planning in deep regional hyperthermia, IEEE Trans Microwave Theory Tech 39 (1991), 864–872.

A. Tannus and M. Garwood, Adiabatic pulses, NMR Biomed 10 (1997), 423–434.

I. Tkac, P. Andersen, G. Adriany, H. Merkle, K. Ugurbil, and R. Gruetter, In vivo 1H NMR spectroscopy of the human brain at 7 T, Magn Reson Med 46 (2001), 451–456.

P.F. van de Moortele, C. Akgun, G. Adriany, S. Moeller, J. Ritter, C.M. Collins, M.B. Smith, J.T. Vaughan, and K. Ugurbil, B1 destructive interferences and spatial phase patterns at 7 T with a head transceiver array coil, Magn Reson Med 54 (2005), 1503–1518.

J.T. Vaughan, H.P. Hetherington, J.O. Otu, J.W. Pan, and G.M. Pohost, High frequency volume coils for clinical NMR imaging and spectroscopy, Magn Reson Med 32 (1994), 206–218.

T. Vaughan, L. DelaBarre, C. Snyder, J. Tian, C. Akgun, D. Shrivastava, W. Liu, C. Olson, G. Adriany, J. Strupp, P. Andersen, A. Gopinath, P.F. van de Moortele, M. Garwood, and K. Ugurbil, 9.4T human MRI: Preliminary results, Magn Reson Med 56 (2006), 1274–1282.

J. Wang, Q.X. Yang, X. Zhang, C.M. Collins, M.B. Smith, X.H. Zhu, G. Adriany, K. Ugurbil, and W. Chen, Polarization of the RF field in a human head at high field: A study with a quadrature surface coil at 7.0 T, Magn Reson Med 48 (2002), 362–369.

Z. Wang, J.C. Lin, W. Mao, W. Liu, M.B. Smith, and C.M. Collins, SAR and temperature: Simulations and comparison to regulatory limits for MRI, J Magn Reson Imaging 26 (2007), 437–441.

M. Weihrauch, P. Wust, M. Weiser, J. Nadobny, S. Eisenhardt, V. Budach, and J. Gellermann, Adaptation of antenna profiles for control of MR guided hyperthermia (HT), in a hybrid MR-HT system, Med Phys 34 (2007), 4717–4725.

F. Wiesinger, P. Boesiger, and K.P. Pruessmann, Electrodynamics and ultimate SNR in parallel MR imaging, Magn Reson Med 52 (2004a), 376–390.

F. Wiesinger, P.F. van de Moortele, G. Adriany, Z.N. De, K. Ugurbil, and K.P. Pruessmann, Parallel imaging performance as a function of field strength—An experimental investigation using electrodynamic scaling, Magn Reson Med 52 (2004b), 953–964.

F. Wiesinger, P.F. van de Moortele, G. Adriany, Z.N. De, K. Ugurbil, and K.P. Pruessmann, Potential and feasibility of parallel MRI at high field, NMR Biomed 19 (2006), 368–378.

G.C. Wiggins, C. Triantafyllou, A. Potthast, A. Reykowski, M. Nittka, and L.L. Wald, 32-Channel 3 tesla receive-only phased-array head coil with soccer-ball element geometry, Magn Reson Med 56 (2006), 216–223.

G.C. Wiggins, J.R. Polimeni, A. Potthast, M. Schmitt, V. Alagappan, and L.L. Wald, 96-Channel receive-only head coil for 3 Tesla: Design optimization and evaluation, Magn Reson Med 62 (2009), 754–762.

S.M. Wright, R.L. Magin, and J.R. Kelton, Arrays of mutually coupled receiver coils: Theory and application, Magn Reson Med 17 (1991), 252–268.

P. Wust, J. Nadobny, R. Felix, P. Deuflhard, A. Louis, and W. John, Strategies for optimized application of annular-phased-array systems in clinical hyperthermia, Int J Hyperthermia 7 (1991), 157–173.

E. Yacoub, A. Shmuel, J. Pfeuffer, P.F. van de Moortele, G. Adriany, P. Andersen, J.T. Vaughan, H. Merkle, K. Ugurbil, and X. Hu, Imaging brain function in humans at 7 Tesla, Magn Reson Med 45 (2001), 588–594.

Q.X. Yang, J. Wang, X. Zhang, C.M. Collins, M.B. Smith, H. Liu, X.H. Zhu, J.T. Vaughan, K. Ugurbil, and W. Chen, Analysis of wave behavior in lossy dielectric samples at high field, Magn Reson Med 47 (2002), 982–989.

A.C. Zelinski, L.L. Wald, K. Setsompop, V. Alagappan, B.A. Gagoski, V.K. Goyal, and E. Adalsteinsson, Fast slice-selective radio-frequency excitation pulses for mitigating B1+ inhomogeneity in the human brain at 7 tesla, Magn Reson Med 59 (2008), 1355–1364.

X.Z. Zhang and A. Webb, Design of a capacitively decoupled transmit/receive NMR phased array for high field microscopy at 14.1 T, J Magn Reson 170 (2004), 149–155.

J.J. Zwanenburg, J. Hendrikse, T. Takahara, F. Visser, and P.R. Luijten, MR angiography of the cerebral perforating arteries with magnetization prepared anatomical reference at 7 T: Comparison with time-of-flight, J Magn Reson Imaging 28 (2008), 1519–1526.